The OWLeS IOP2b Lake-Effect Snowstorm: Shoreline Geometry and the Mesoscale Forcing of Precipitation

W. JAMES STEENBURGH AND LEAH S. CAMPBELL

Department of Atmospheric Sciences, University of Utah, Salt Lake City, Utah

ABSTRACT

Long-lake-axis-parallel (LLAP) lake-effect precipitation systems that form when the flow is parallel to the long axis of an elongated body of water frequently produce intense, highly localized snowfall. Conceptual models of these LLAP systems typically emphasize the role of thermally forced land breezes from the flanking shorelines, with low-level convergence and ascent centered near the lake axis. In reality, other factors such as shoreline geometry and differential surface roughness can strongly influence LLAP systems. Here a WRF Model simulation is used to examine the mesoscale forcing of lake-effect precipitation over Lake Ontario during IOP2b of the Ontario Winter Lake-effect Systems (OWLeS) field campaign. In the simulation, the large-scale flow, shoreline geometry, and differential surface heating and roughness contribute to the development of three major airmass boundaries. The first is a land-breeze front that forms along a bulge in the south shoreline between St. Catharines, Ontario, Canada, and Thirty Mile Point, New York; extends downstream over eastern Lake Ontario; and plays a primary role in the LLAP system development. The second is a land-breeze front that forms along the southeast shoreline near Oswego, New York; extends downstream and obliquely across the LLAP system near Tug Hill; and influences inland precipitation processes. The third is a convergence zone that extends downstream from the north shoreline near Point Petre, Ontario, Canada; and contributes to the intermittent development of lake-effect precipitation north of the primary LLAP system. These results highlight the multifaceted nature of LLAP system development over Lake Ontario, especially the contributions of shoreline geometry and mesoscale airmass boundaries.

1. Introduction

Accurate prediction of the timing, location, and intensity of lake-effect snowfall is paramount for forecasters in lake-, sea-, and ocean-effect (hereafter simply lake effect) regions. Intense, often highly localized lake-effect snowfall can produce rapid and extreme accumulations, adversely impacting transportation, commerce, and property (Norton and Bolsenga 1993; Schmidlin 1993; Kunkel et al. 2002). Especially strong lake-effect systems (i.e., complexes of lake-effect convection organized on scales larger than individual cells or bands) can be generated during periods of relatively cold flow along the long axis of elongated lakes such as Lake Ontario in eastern North America (Peace and Sykes 1966; Reinking et al. 1993; Ballentine et al. 1998; Steiger et al. 2013; Veals and Steenburgh 2015; Kristovich et al. 2017). These long-lake-axis-parallel (LLAP) systems have produced snowfall rates as high

as 30.5 cm (12 in.) in 1 h, storm-total accumulations of 358 cm (141 in.) in 10 days, and seasonal accumulations of 1173 cm (462 in.) on Tug Hill east of the lake (Burt 2007; Veals and Steenburgh 2015).

Conceptual models of LLAP systems often feature symmetrical land breezes from the flanking shorelines with low-level convergence, ascent, and snowband formation near the midlake axis [e.g., Lackmann (2011), see his Fig. 9.19; Steenburgh (2014), see his Fig. 5.5]. A variety of factors can, however, alter this depiction including the influence of upstream water bodies, direction and strength of the large-scale flow, shoreline geometry, differential surface heating and roughness, and orographic effects (e.g., Passarelli and Braham 1981; Hjelmfelt 1990; Laird et al. 2003a,b; Alcott and Steenburgh 2013). For example, bays and coastline concavities are preferred regions for snowband initiation due to thermally forced convergence (e.g., Atlas et al. 1983; Andersson and Gustafsson 1994; Mazon et al. 2015). During geostrophic flow along an elongated lake, differential surface roughness between the lake and land favors convergence on the right (streamwise) shoreline

---

FIG. 1. Topography and geographic landmarks of the study region. Elevation (m) shaded following inset scale. White line denotes international border between Ontario (ON), Canada, and New York (NY), United States. (Created at maps-for-free.com.)

and divergence on the left rather than at the lake axis [Markowski and Richardson (2010), see their Fig. 4.24]. Based on early numerical simulations of lake-effect systems over Lake Erie, Lavoie (1972) emphasized that "roughness differences between lake and land, topography, latent heat release, and surface heating over the lake all make significant and complimentary contributions in lake-effect situations" (p. 1039).

The relative contributions of differential thermal and roughness forcing are, however, situationally dependent. In real-data numerical simulations of snowbands over the English Channel and Irish Sea, Norris et al. (2013) found that differential roughness (and orography) was less important than thermal forcing for band formation, but did affect location and morphology. Idealized numerical simulations suggest land-breeze-forced ascent during cold-air outbreaks, which often leads to lake-effect band development, is sensitive to wind speed, flow orientation relative to the shore, lake geometry, and lake or sea state (e.g., Laird et al. 2003a,b; Savijärvi 2012, 2015). Over the Great Salt Lake, funneling of the flow into the Salt Lake valley can strongly enhance some LLAP systems, but has little impact on others (e.g., Onton and Steenburgh 2001; Alcott and Steenburgh 2013).

Although having a general oval shape, the shoreline of Lake Ontario includes several undulations that could influence the formation, location, and intensity of LLAP systems (Fig. 1). These undulations include a bulge in the south shoreline between St. Catharines, Ontario, Canada, and Rochester, New York; a bulge in the

southeast shore near Oswego, New York; and an irregular peninsula in the north shore extending to Point Petre (hereafter the entire peninsula will be referred to as Point Petre). Holroyd (1971) distinguished between lake-effect storms that formed near the long axis of Lake Ontario, which he classified as "thermally induced," and those that form near the south shore bulge between St. Catharines and Rochester, which he classified as "friction induced." He identified the south shore bulge as a preferred region for snowband development. Along the bulge in the southeast shore near Oswego, Peace and Sykes (1966) identified a broad zone of confluence and convergence that fed into the broader region of confluence and convergence beneath a LLAP system, but did not explore its possible role in the storm evolution.

During December 2013 and January 2014, the Ontario Winter Lake-effect Systems (OWLeS) field program investigated lake-effect storms generated by Lake Ontario (Kristovich et al. 2017). Intensive observing period 2b (IOP2b) examined an intense LLAP system that produced 101.5 cm of snow in 24 h on Tug Hill east of Lake Ontario. While previous studies describe the structure and characteristics of the LLAP system over eastern Lake Ontario and Tug Hill (Minder et al. 2015; Campbell et al. 2016; Welsh et al. 2016; Bergmaier et al. 2017), the present paper examines the mesoscale forcing of the LLAP system with emphasis on the role of the shoreline geometry, which played an unexpectedly prominent role in simulations exploring orographic effects over Tug Hill (Campbell and Steenburgh 2017). In the next section, we describe the datasets and modeling

system used for our analysis. Sections 3–6 then use operational analyses, Weather Research and Forecasting (WRF) Model simulations, trajectories, and frontogenesis diagnostics to show how the large-scale flow, shape of the Lake Ontario shoreline, and differential surface heating and roughness contribute to the development of three major airmass boundaries that influence the LLAP system development and evolution. A summary and conclusions are presented in section 7, including a discussion of the significance of these findings for operational forecasting and our understanding of lake-effect precipitation processes.

2. Data and methods

a. Regional analyses and observational datasets

Regional analyses come from the operational Rapid Refresh (RAP; 13-km grid spacing; Benjamin et al. 2016), obtained from the NOAA National Operational Model Archive and Distribution System (NOMADS) at the National Centers for Environmental Information (NCEI), and the High-Resolution Rapid Refresh (HRRR; 3-km grid spacing; Smith et al. 2008; Benjamin et al. 2016), provided by the NOAA/Earth System Research Laboratory. During the study period, the HRRR was not yet operational and was not available prior to 1200 UTC 11 December. Hence, we use the RAP prior to this time and the HRRR thereafter.

Radar reflectivity analyses include lowest-elevation scans from the National Weather Service Buffalo (KBUF), Montague (KTYX), and Binghamton (KBGM), New York, WSR-88Ds, as well as the Environment and Climate Change Canada King City Radar (WKR). The WSR-88Ds operate with a 10-cm wavelength and 0.5° lowest-elevation scan, whereas WKR operates with a 5-cm wavelength and 0.2° lowest-elevation scan. Although these radars provide regional coverage, they can overshoot shallow lake-effect convection in some areas, especially over central Lake Ontario (see Brown et al. 2007). The WSR-88D data were obtained from the NCEI Next Generation Weather Radar (NEXRAD) archive in level-II format (Crum et al. 1993), whereas the WKR data were obtained from the National Center for Atmospheric Research/Earth Observing Laboratory (NCAR/EOL) OWLeS dataset catalog.

b. WRF modeling

We examine IOP2b using the WRF Model control simulation described by Campbell and Steenburgh (2017), who investigated the mechanisms responsible for the Tug Hill precipitation maximum during IOP2b. The simulation includes domains with 12-, 4-, and 1.3-km grid spacing [see Fig. 1 of Campbell and Steenburgh (2017) for nesting configuration and topography], 36 vertical levels with 8 levels at or below 1 km AGL, and a parameterization suite that includes the Rapid Radiative Transfer Model longwave radiation scheme (Iacono et al. 2008), Dudhia shortwave radiation scheme (Dudhia 1989), Noah land surface model (Chen and Dudhia 2001), Yonsei University planetary boundary layer parameterization with a revised surface layer scheme (Hong et al. 2006; Jiménez et al. 2012), Kain–Fritsch-2 cumulus parameterization (Kain 2004; 12-km domain only), and Thompson cloud microphysics parameterization (Thompson et al. 2008). Land use derives from U.S. Geological Survey land-use data and around Lake Ontario consists primarily of deciduous broadleaf forest, dryland cropland and pasture, and cropland/grassland mosaic, with pockets of urban and built-up land, grassland, and mixed forest (not shown). Analyses from the NCEP North American Mesoscale Forecast System (NAM) provide initial atmospheric and land surface (soil moisture, soil temperature, and snow cover) conditions at 1200 UTC 10 December 2013, as well as lateral boundary conditions at 6-h intervals throughout the study period. For Great Lakes surface temperatures, we use the Great Lakes Environmental Research Laboratory (GLERL) Great Lakes Coastal Forecasting System analysis at 6-h intervals. In areas where the WRF shoreline lays farther inland than the GLERL analysis, we set the lake-surface temperature to 0°C. Ice cover and temperatures of smaller lakes are specified manually as described in Campbell and Steenburgh (2017).

3. Event overview

As described by Campbell et al. (2016) and Campbell and Steenburgh (2017), IOP2b featured a 24-h period of heavy lake-effect snowfall (0000 UTC 11 December–0000 UTC 12 December 2013) that produced 101.5 cm of snow at the University of Utah observing site on the western slope of Tug Hill. For most of IOP2b, the large-scale flow was approximately parallel to the long axis of Lake Ontario, and the mode of lake-effect precipitation features produced by the resulting LLAP system fluctuated between broad coverage and intense LLAP bands. At times, a secondary snowband formed over northeast Lake Ontario.

The RAP surface analysis at 0600 UTC 11 December shows predominantly west-northwesterly geostrophic flow with cross-isobar southwesterly winds north of Lake Ontario (Fig. 2a). Over Lake Ontario the flow is stronger, a likely consequence of reduced surface drag
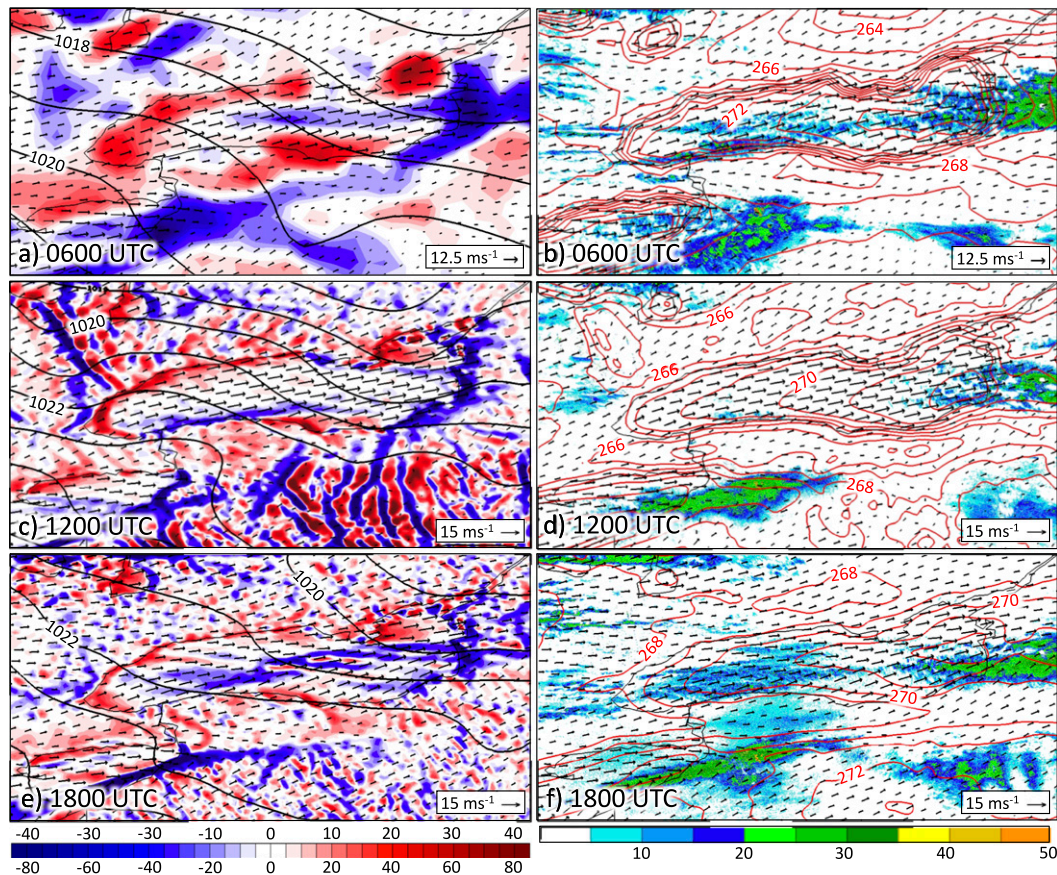
FIG. 2. (a) RAP analysis of sea level pressure (contours every 1 hPa), 10-m wind vectors (following inset scale), and divergence [$\times 10^{-5}\,\mathrm{s}^{-1}$ following scale at bottom (top labels)] at 0600 UTC 11 Dec. (b) Lowest-elevation scan reflectivity from the KBUF, KTYX, KBGM, and WKR radars (dBZ following scale at bottom) with RAP 2-m potential temperature (contours every 1 K) and 10-m wind vectors [as in (a)] at 0600 UTC 11 Dec. (c),(d) As in (a),(b), but for HRRR analysis at 1200 UTC 11 Dec and with the divergence scale based on lower labels. Potential temperature smoothed with a seven-point cowbell spectral filter (Barnes et al. 1996) for clarity. (e),(f) As in (a),(b), but for HRRR analysis at 1800 UTC 11 Dec.

and deeper momentum mixing within the lake-effect convective boundary layer (Kristovich et al. 2003; Schroeder et al. 2006). South of Lake Ontario, the flow is once again weaker due to the greater drag and a weaker pressure gradient over the Lake Ontario lowlands. The overall wind pattern exhibits divergence in areas where the flow is offshore and accelerates from over land to over water, or parallel to the shore with land to the left, which yields directional divergence due to differential drag. These areas include most of the western and northern shore from St. Catharines to Brighton and the southern shore from Thirty Mile Point to Sodus Bay. Conversely, the flow exhibits convergence where the flow is onshore or parallel to the shore with land on the right. These areas include the south shore between St. Catharines and Thirty Mile Point, the southeast shore near Oswego, and the north shore west of Point Petre.

Radar imagery at this time reveals weak wind-parallel bands, presumably generated by Lake Huron, extending downstream to the west shore of Lake Ontario (Fig. 2b). Over western Lake Ontario, a stronger wind-parallel band extends along the south shore from St. Catharines to Thirty Mile Point. This shoreline band is roughly collocated with the aforementioned surface convergence, as well as concomitant baroclinity along this section of the shoreline (cf. Figs. 2a,b). Just to the north, lake-effect precipitation also occurs near the long-lake axis and within the core of highest surface potential temperatures. These precipitation features weaken over central Lake Ontario, although this likely reflects radar overshooting. Despite the poor sampling, radar echoes associated with the shoreline band extend quasi-continuously downstream, eventually connecting with the LLAP system over eastern Lake Ontario, which is better sampled by the KTYX radar. Over northeastern Lake

Ontario, a secondary area of lake-effect precipitation extends east-southeastward from Point Petre, merging with the primary LLAP system near the east shore.

The kinematic features noted above persist through 1200 UTC 11 December when the 3-km HRRR analysis provides a higher-resolution perspective that better resolves near-coast effects and other smaller-scale features (Fig. 2c, the scales used for divergence differ due to the varying resolutions of the models). Consistent with the earlier RAP analysis, the HRRR produces divergence along most of the western and northern shore from St. Catharines to Brighton and the southern shore from Thirty Mile Point to Sodus Bay. These are areas with offshore or shore-parallel flow with land to the left. Also consistent with the earlier RAP analysis, the HRRR produces convergence along the south shore from St. Catharines to Thirty Mile Point, the southeast shore near Oswego, and the north shore west of Point Petre. These are areas with onshore or shore-parallel flow with land to the right.

Radar imagery shows the LLAP system is weaker at this time with only weak echoes along the south shore bulge from St. Catharines to Thirty Mile Point and disorganized broad coverage over eastern Lake Ontario and Tug Hill (Fig. 2d). Radar echoes over central Lake Ontario are nonexistent. Campbell et al. (2016) show that during this period the lake-effect convective boundary layer and radar echo depths are the shallowest of the event [echo tops ~2300 m MSL as inferred from profiling radars; see Fig. 7 of Campbell et al. (2016)], so the lack of returns over central Lake Ontario likely reflects overshooting.

The large-scale pressure gradient weakens through 1800 UTC as a weak surface cold front approaches Lake Ontario from the north (Fig. 2e). The lake–land temperature contrast and associated coastal temperature gradients also weaken as temperatures surrounding the lake increase with daytime surface heating (Fig. 2f). Concurrently, shoreline divergence and convergence weaken in most areas while convergence strengthens near the long-lake axis, especially over eastern Lake Ontario (Fig. 2e). Nevertheless, the LLAP system strengthens, presumably due to a deepening of the lake-effect convective boundary layer (see Campbell et al. 2016), yielding an intense LLAP band over eastern Lake Ontario that extends inland over Tug Hill (Fig. 2f). During this period, precipitation rates on Tug Hill were the highest of the event (see Campbell et al. 2016). Using data collected by the University of Wyoming King Air research aircraft over eastern Lake Ontario, Bergmaier et al. (2017) describe the mesoscale structure of the LLAP band over eastern Lake Ontario and the windward slope of Tug Hill. Careful inspection of the radar

imagery also reveals weaker lake-effect precipitation just to the north of the primary LLAP system, with a possible connection to Point Petre. Heavy snowfall continued east of Lake Ontario through ~2200 UTC when the LLAP system shifted southward with the approach and passage of the cold front (not shown). The event ended at ~0300 UTC 12 December.

The analysis described above suggests that the orientation of the large-scale flow relative to the shoreline modulates the distribution of divergence around Lake Ontario. In this case, the south shore bulge between St. Catharines and Thirty Mile Point, southeast shoreline near Oswego, and Point Petre appear to be favored areas for airmass boundaries and associated low-level convergence that ultimately affect the development of lake-effect precipitation. We now explore this possibility in greater depth using the WRF simulation.

4. WRF simulation

Campbell and Steenburgh (2017) provide a comprehensive validation of the WRF simulation downstream of Lake Ontario, including the distribution and magnitude of precipitation (liquid precipitation equivalent) over Tug Hill. They found that the simulated precipitation closely matched observed, with a slight southward displacement of the axis of maximum precipitation. Our focus here is on the mesoscale forcing of the LLAP system over and around Lake Ontario.

At 0600 UTC 11 December, the 1.3-km WRF domain features a surface (i.e., lowest-half-η level) convergence zone that develops along the south shore bulge between St. Catharines and Thirty Mile Point (Fig. 3a). The surface potential temperature analysis shows that this convergence is associated with a land-breeze front that separates lake-modified air from a tongue of cooler air over the lowlands south of Lake Ontario (Fig. 3b, hereafter LBF1). Although typically associated with the leading edge of denser, cooler air during offshore flow at night and in the early morning, we use the term land-breeze front here since it has traditionally been used in the lake-effect literature to describe airmass boundaries generated by differential surface heating over the Great Lakes during winter (e.g., Passarelli and Braham 1981; Schoenberger 1984; Hjelmfelt 1990; Grim et al. 2004). We note, however, that LBF1 bears many similarities to coastal fronts that form along the U.S. East Coast and other regions of the world (e.g., Bosart et al. 1972; Bosart 1975; Davis and Lee 2012; Lee and Xue 2013). Cross section W–W' highlights the ~2-K temperature contrast and narrow ascent plume associated with LBF1 (Fig. 4a). The ascent generates a band of clouds and an elevated reflectivity maximum, which is displaced a few
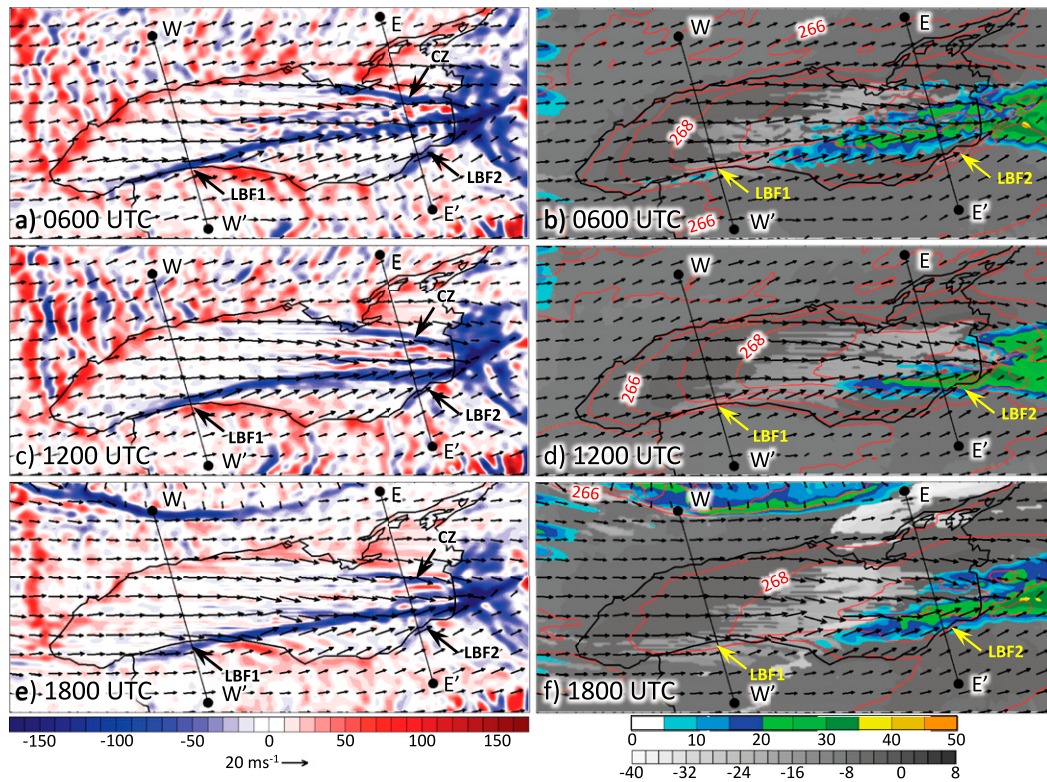
FIG. 3. (a) WRF 1.3-km lowest-half-η-level wind (vectors following scale at bottom) and lowest-half-η-level divergence ($\times 10^{-5}$ s^{-1} following scale at bottom) at 0600 UTC 11 Dec. Divergence smoothed with a seven-point cowbell spectral filter (Barnes et al. 1996) for clarity. (b) WRF 1.3-km lowest-half-η-level potential temperature (contours every 1 K), lowest-half-η-level wind [as in (a)], cloud-top temperature (°C following gray-shaded scale at bottom), and lowest-half-η-level reflectivity (dBZ following color scale at bottom) at 0600 UTC 11 Dec. Potential temperature smoothed with a seven-point cowbell spectral filter (Barnes et al. 1996) for clarity. (c),(d) As in (a),(b), but for 1200 UTC 11 Dec. (e),(f) As in (a),(b), but for 1800 UTC 11 Dec. Positions of cross sections W–W′ and E–E′ are annotated.

kilometers inland because the large-scale flow aloft has slight onshore component at this location.

LBF1 detaches from the shore near Thirty Mile Point. Although the baroclinity weakens, strong convergence extends downstream over central and eastern Lake Ontario and serves as the locus for development of the predominant precipitation band produced by the simulation (Figs. 3a,b). Over eastern Lake Ontario, a second land-breeze front and associated low-level convergence exists along the southeast shore near Oswego (hereafter LBF2). Convergence and baroclinity associated with LBF2 extends inland across Tug Hill and obliquely across the predominant precipitation band. Meanwhile, along the north shore, convergence develops near Point Petre and extends downstream across Lake Ontario (labeled CZ in Fig. 3a).

Analysis of the surface (i.e., lowest-half-η level) potential temperature gradient at this time highlights the three major airmass boundaries described above (Fig. 5a). Elongated maxima exist along the south shore

bulge and southeast shore and extend downstream, with the former weakening over eastern Lake Ontario and the latter achieving maximum strength just inland of the Lake Ontario shore before weakening further inland. An elongated maximum in potential temperature gradient is also collocated with the convergence zone downstream of Point Petre. We elect not to classify this boundary as a land-breeze front, however, given the weaker, less organized nature of the baroclinity.

Cross section E–E′ reveals the relationship of these boundaries to the lake-effect system over eastern Lake Ontario at this time (Fig. 4b). The southernmost simulated radar reflectivity maximum is associated with the narrow plume of ascent produced by the convergence associated with the downstream extension of LBF1. This band is clearly distinct from LBF2 (position denoted by black arrow). The northernmost maximum, which is weak and barely reaches the surface (see also Fig. 3b), forms along the convergence zone that extends downstream from Point Petre. In between these maxima is
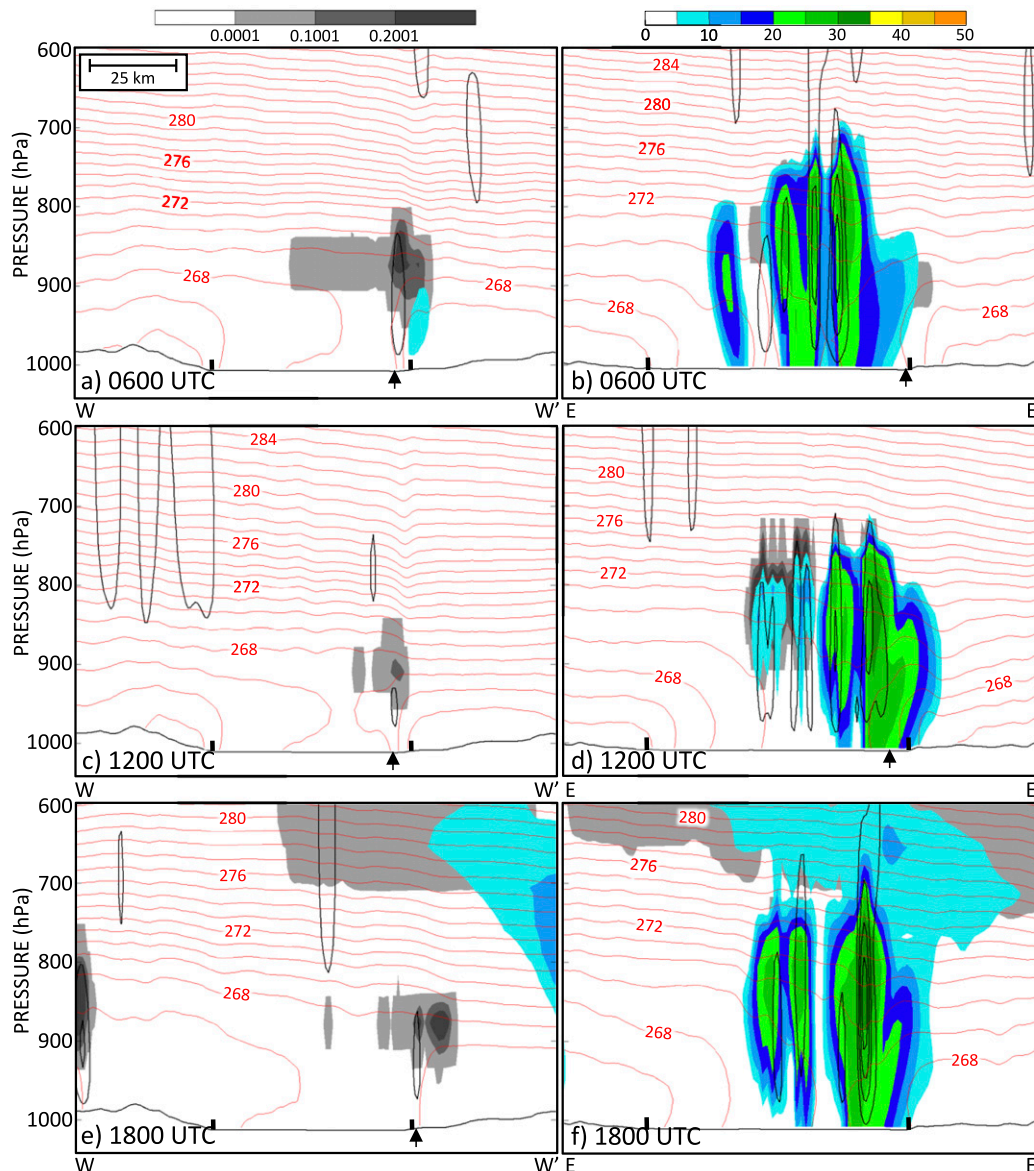
FIG. 4. Cross sections along lines W–W′ and E–E′ of Fig. 3. (a) Potential temperature (red contours every 1 K), vertical velocity (black contours every 50 cm s^{-1} beginning at 25 cm s^{-1}), combined cloud water and ice mixing ratio (g kg^{-1} following gray-shaded scale at top left), and model-derived radar reflectivity (dBZ following color scale at top right, covers cloud water and ice mixing ratio analysis) along W–W′ at 0600 UTC 11 Dec. Potential temperature and vertical velocity smoothed with a seven-point cowbell spectral filter (Barnes et al. 1996) for clarity. (b) As in (a), but along E–E′. (c),(d) As in (a),(b), but at 1200 UTC 12 Dec. (e),(f) As in (a),(b), but at 1800 UTC 12 Dec. Approximate position of LBF2 identified with arrow when well defined. Horizontal distance scale at top left of (a). Shorelines are identified with black tick marks.

another area of lake-effect precipitation that is not associated with a surface airmass boundary.

The three airmass boundaries persist through 1200 and 1800 UTC, with some variations in structure and intensity. First, the downstream extension of LBF1 and associated convergence shift slightly southward and become less distinct from LBF2 (cf. Figs. 3a,c,e). Second, the strength of the land–lake temperature

difference maximizes at 1200 UTC in response to nocturnal cooling and then weakens through 1800 UTC in response to daytime heating (cf. Figs. 3b,d,f). Concurrently, cross section W–W′ shows that the temperature contrast across LBF1 reaches maximum strength at 1200 UTC and then weakens through 1800 UTC (cf. Figs. 4a,c,e). Strengthening of LBF2 is less apparent in cross section E–E′ at 1200 UTC, but weakening
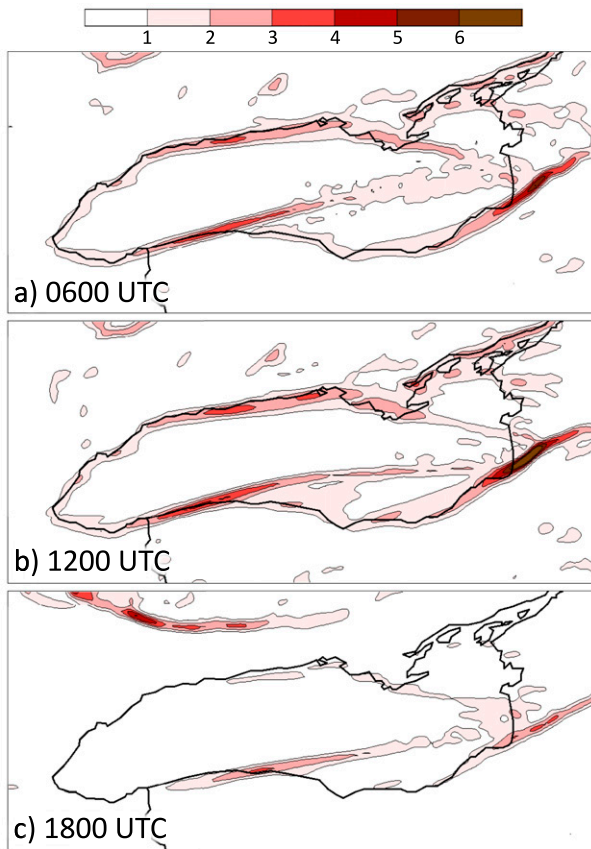
FIG. 5. Magnitude of the WRF lowest-half-η-level horizontal potential temperature gradient [K $(10\,km)^{-1}$ following color scale at top] at (a) 0600, (b) 1200, and (c) 1800 UTC 11 Dec.

is clear at 1800 UTC (cf. Figs. 4b,d,f). This diurnal modulation of the land-breeze front baroclinity is also evident in surface potential temperature gradient analyses, which show the three airmass boundaries persist through the period, reaching maximum intensity at 1200 UTC (Fig. 5b) and weakening by 1800 UTC (Fig. 5c). Throughout this period, the downstream extension of LBF1 and associated convergence remains the dominant driver of precipitation.

In general, these characteristics of the WRF simulation show reasonable correspondence to analyses and radar images of IOP2b. In particular, the WRF simulation shows the development of airmass boundaries in areas where the flow is onshore or parallel to the shore with land on the right, with land-breeze fronts developing along the south shore bulge (LBF1) and southeast shore (LBF2). In contrast, divergence occurs in areas where the flow is offshore or parallel to the shore with land on the left. Less well simulated are three aspects of the observed event. The first is a lack of simulated precipitation features extending downstream

from Lake Huron to Lake Ontario, as seen at times in the observed event (cf. Figs. 2b,d,f and 3b,d,f). The second is the strength and persistence of the simulated predominant precipitation band, which exhibited a banded structure even at times when the observed banding was weak or limited [cf. Figs. 2d and 3d; see also Campbell and Steenburgh (2017)]. McMillen and Steenburgh (2015) show that WRF simulations of Great Salt Lake–effect precipitation events produced at the same grid spacing (1.3 km) frequently produce banded features when nonbanded features are observed, suggesting this may be an inherent bias of the WRF Model, the model physics used, or simulations that do not explicitly resolve boundary layer turbulence and are thus dominated by mesoscale ascent. Finally, the scale and structure of precipitation features produced by the WRF do not reflect the full spectrum of that observed, especially smaller-scale open-cellular convection. We focus hereafter on those aspects of the event that are reasonably resolved and evident in analyses of the event, especially the airmass boundaries and their influence on precipitation development during the event.

5. Trajectories

Trajectories ending on the lowest-half-η level along W–W′, E–E′, and an intermediate transect help illustrate how the coastal geometry and differential trajectory residence times over Lake Ontario affect the development of the airmass boundaries described above (Fig. 6). We focus on trajectories ending at 1200 UTC, when the lake–land temperature contrast is strongest, and 1800 UTC, when the lake–land temperature contrast is weaker due to daytime heating over land. Results at 0600 UTC are qualitatively similar to 1200 UTC.

Trajectories ending at 1200 UTC enter the 1.3-km domain from the western boundary and cluster into three categories based on trajectory paths and thermodynamic evolutions. The first category includes trajectories that cross the west coast of Lake Ontario, experience long overwater residence times, and form the core of the warm anomaly over Lake Ontario (red trajectories, Fig. 6a). Time series show an abrupt increase in potential temperature along these trajectories as they move over Lake Ontario, with continued warming as they remain over water (Figs. 6b–d). The second category includes trajectories that remain predominantly over land initially, but eventually move over water near Point Petre on the north shore (light orange trajectories) or between Thirty Mile Point and Oswego on the south shore (orange trajectories). The potential
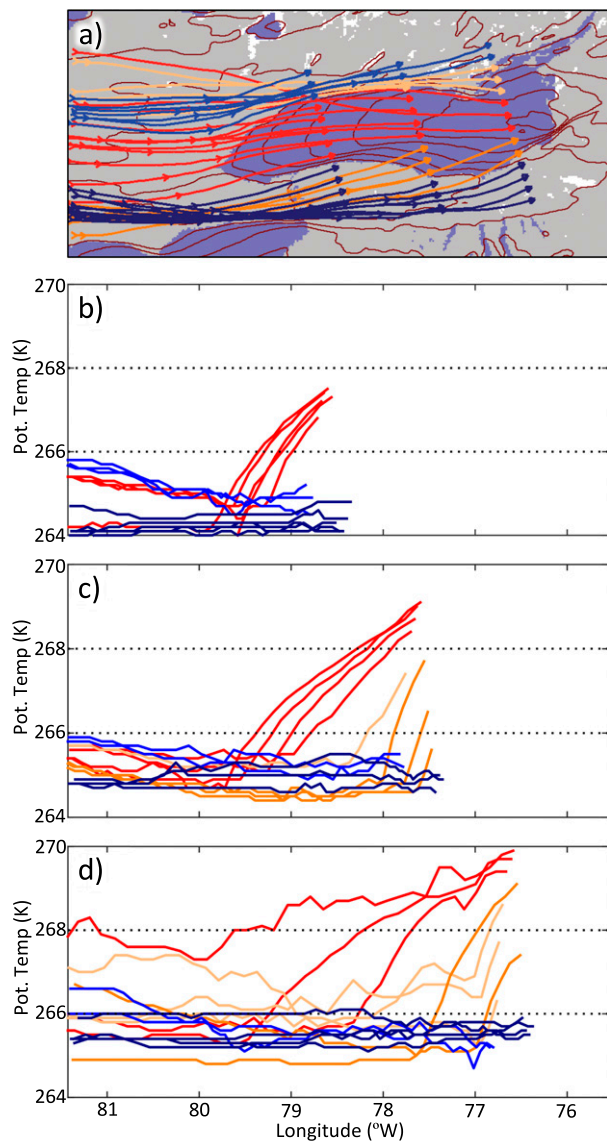
FIG. 6. (a) Trajectories ending on the lowest-half-η level, lowest-half-η-level potential temperature (contours every 1 K, unlabeled), and WRF land surface characteristics (light blue = water, ice = white, land = gray) at 1200 UTC 11 Dec. Potential temperature smoothed with a seven-point cowbell spectral filter (Barnes et al. 1996) for clarity. (b) Potential temperature along trajectories ending at the westernmost transect (corresponding to W–W′ of Fig. 3). (c) Potential temperature along trajectories ending at the intermediate transect. (d) Potential temperature along trajectories ending at the easternmost transect (corresponding to E–E′ of Fig. 3).

temperature along these trajectories also increases abruptly as they move over Lake Ontario, but the total increase in potential temperature is smaller than along trajectories that form the core of the warm anomaly over Lake Ontario due to the shorter overwater residence times. The third category includes trajectories that

remain predominantly or entirely over land north (blue trajectories) or south (dark blue trajectories) of Lake Ontario and experience little to no lake modification. The trajectories south of Lake Ontario pass through the land bridge between Lakes Erie and Ontario and form a cold tongue over the Lake Ontario lowlands. The potential temperature along these predominantly overland trajectories remains nearly constant or decreases slightly. Air to the south of the cold tongue has been modified by Lake Erie and is warmer (trajectories not shown).

The trajectories and their thermodynamic histories described above help explain some of the variations in the intensity of baroclinity along the Lake Ontario shoreline. Along the south shore bulge between St. Catharines and Thirty Mile Point, LBF1 represents an abrupt transition between trajectories with long residence times over Lake Ontario and those that have moved through the land bridge between Lakes Erie and Ontario and have experienced no lake modification, leading to a strong temperature gradient near the coast along W–W′ (Figs. 5b and 6a,b). Farther downstream over Lake Ontario, the southward dip in the shoreline results in a more gradual transition in the overwater residence time and lake modification, yielding a broader transition in temperature along trajectories ending along the intermediate transect (Figs. 6a,c). Over eastern Lake Ontario, however, the shoreline once again becomes oriented along the flow, resulting once again in a sharper contrast in overwater residence time and lake modification and a stronger temperature gradient near the coast along E–E′ (Figs. 6a,d).

Although such trajectory contrasts are also evident along the north shoreline, the magnitude of the horizontal potential temperature gradient is weaker than found near the south shore bulge or southeastern shore (Fig. 5b). In part, this reflects the divergent, frontolytical nature of the flow along most of the north coast (Fig. 3), as discussed in section 6.

The general characteristics of the trajectories and the temperature analysis over and surrounding Lake Ontario persist with little change through 1800 UTC, with one notable exception (Fig. 7). Instead of experiencing no change or a slight decrease in potential temperature, trajectories experience an increase in potential temperature while over land after ~1300 UTC due to diurnal heating. For example, the potential temperature of trajectories remaining over land south of Lake Ontario (dark blue trajectories) increases ~2.5 K. This weakens the temperature gradients near the north shore, south shore bulge, and southeastern shore.
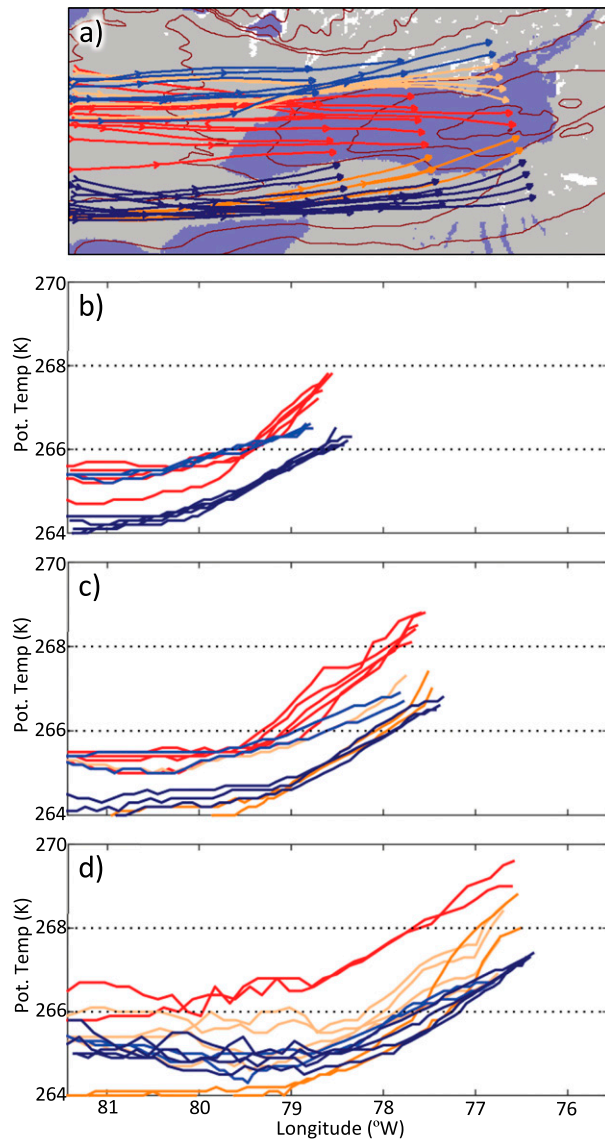
FIG. 7. As in Fig. 6, but for 1800 UTC 11 Dec.

6. Frontogenesis diagnostics

Previous numerical and observational studies reveal an intensification of the temperature gradient, convergence, and ascent accompanying land- and sea-breeze fronts when a large-scale flow of modest strength opposes the thermally forced flow (e.g., Arritt 1993; Miller et al. 2003; Case et al. 2005; Crosman and Horel 2010). In such situations, a positive feedback loop between the convergent frontogenesis and strengthening front leads to the stronger temperature gradient and frontal circulation (Arritt 1993). In contrast, land- and sea-breeze fronts are typically weaker when the large-scale flow is in the same direction as the thermally forced flow since this weakens convergent frontogenesis or produces

frontolysis. The response in situations when the large-scale flow is parallel to the coast is less clear, but in the case of a land- or sea-breeze front, convergence produced by differential surface roughness along the streamwise-right shore of a lake [e.g., Alestalo and Savijärvi (1985); Markowski and Richardson (2010), see their Fig. 4.24] would produce frontogenesis, whereas divergence produced by differential surface roughness along the streamwise-left shore of a lake would produce frontolysis.

The analysis presented above, which highlights the development of convergence in areas with onshore flow or shore-parallel flow along the streamwise right (south) shore, suggests that such effects play an important role in land-breeze development and the mesoscale forcing of lake-effect precipitation during IOP2b. To examine this possibility, we examine frontogenesis F on the WRF lowest-half-η level, defined following Petterssen (1936) and Miller (1948) as

$$F = \frac{d}{dt}|\nabla_\eta \theta|,$$

where

$$\frac{d}{dt} = \frac{\partial}{\partial t} + u\frac{\partial}{\partial x_\eta} + v\frac{\partial}{\partial y_\eta} + \dot{\eta}\frac{\partial}{\partial \eta},$$

$$\nabla_\eta = \mathbf{i}\frac{\partial}{\partial x_\eta} + \mathbf{j}\frac{\partial}{\partial y_\eta},$$

the subscript η denotes differentiation along the lowest-η level, and $\dot{\eta}$ is the η-coordinate vertical velocity. Following Miller (1948), Eq. (1) may be written as

$$F = F_w + F_T + F_D,$$

where

$$F_w = -\frac{1}{|\nabla_\eta \theta|}\left[\frac{\partial\theta}{\partial x}\left(\frac{\partial u}{\partial x}\frac{\partial\theta}{\partial x} + \frac{\partial u}{\partial y}\frac{\partial\theta}{\partial y}\right) + \frac{\partial\theta}{\partial y}\left(\frac{\partial v}{\partial x}\frac{\partial\theta}{\partial x} + \frac{\partial v}{\partial y}\frac{\partial\theta}{\partial y}\right)\right],$$

$$F_T = -\frac{1}{|\nabla_\eta \theta|}\left[\frac{\partial\theta}{\partial \eta}\left(\frac{\partial\dot{\eta}}{\partial x}\frac{\partial\theta}{\partial x} + \frac{\partial\dot{\eta}}{\partial y}\frac{\partial\theta}{\partial y}\right)\right],$$

$$F_D = -\frac{1}{|\nabla_\eta \theta|}\left(-\frac{\partial\theta}{\partial x}\frac{\partial}{\partial x}\frac{d\theta}{dt} - \frac{\partial\theta}{\partial y}\frac{\partial}{\partial y}\frac{d\theta}{dt}\right),$$

and the subscript η is dropped for convenience. Here F_w is the frontogenesis produced by horizontal divergence and deformation (hereafter *kinematic frontogenesis*), F_T is the tilting frontogenesis, and F_D is the frontogenesis associated with horizontal gradients in diabatic heating and cooling (hereafter the *diabatic frontogenesis*). We ignore F_T as it is generally small near the surface where
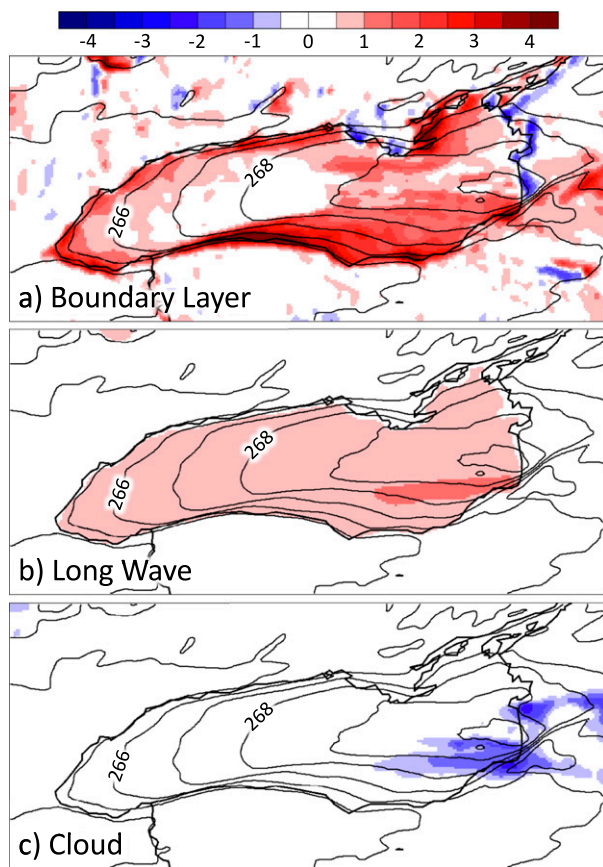
FIG. 8. WRF lowest-half-η-level potential temperature (contours every 1 K) and diabatic heating rates (K h^{-1} following scale at top) produced by the (a) boundary layer, (b) longwave radiation, and (c) cloud microphysics parameterizations at 1200 UTC 11 Dec. Potential temperature and diabatic heating rates smoothed with a seven-point cowbell spectral filter (Barnes et al. 1996) for clarity.

vertical velocity and its horizontal derivatives over relatively smooth terrain are weak, and calculate F_D using diabatic heating rates obtained from the WRF boundary layer, longwave radiation, and cloud microphysics parameterizations. We omit the influence of shortwave heating at the lowest-η level since it is zero at night and negligible during the day (shortwave heating of the land surface and subsequent warming of the lowest-η level by sensible heat fluxes are included in the boundary layer heating rate). We focus on 1200 UTC when the land-breeze fronts are near maximum strength and 1800 UTC when surface heating has weakened the land-breeze fronts.

At 1200 UTC, diabatic heating produced by the boundary layer parameterization is greatest over Lake Ontario, with the highest values near the shore where cold, continental air first moves over the relatively warm lake surface (Fig. 8a). Airmass modification lessens the lake–air temperature contrast leading to smaller heating

rates near the long-lake axis. Longwave heating is also greatest over Lake Ontario, but features weaker maxima than the boundary layer heating (Fig. 8b). Pockets of diabatic cooling produced by the cloud microphysics parameterization occur beneath the simulated lake-effect system over and downstream of eastern Lake Ontario (Fig. 8c, see also Fig. 3d).

Gradients in boundary layer and longwave heating lead to strong diabatic frontogenesis along most of the Lake Ontario shoreline (Fig. 9a). Strong diabatic frontolysis also occurs along the LBF1 offshore of the bulge between St. Catharines and Rochester. Frontolysis in this area may seem counterintuitive but reflects the intense diabatic heating maximum produced immediately behind (south of) LBF1 owing to the movement of cold, continental air over Lake Ontario. Diabatic frontogenesis and frontolysis associated with the cloud microphysics parameterization is found over and downstream of eastern Lake Ontario and is not well phased with any areas of concentrated potential temperature gradient (Fig. 9b).

Kinematic frontolysis counters the diabatic frontogenesis in coastal areas where the flow is offshore or parallel to the shore with land to the left, which leads to speed or directional divergence (Fig. 9c). Kinematic frontogenesis occurs, however, where the flow is onshore or parallel to the coast with land to the right, which leads to speed or directional convergence. The combination of diabatic and kinematic frontogenesis yields banded maxima of total frontogenesis along the south shore bulge between St. Catharines and Thirty Mile Point, which detaches from the shore near Thirty Mile Point and extends downstream near the long-lake axis, and along the southeast shore near Lake Ontario. A weaker, less continuous band of frontogenesis extends downstream from Point Petre. These results indicate that differential diabatic heating combines with differential surface roughness and resulting convergence to produce frontogenesis and land-breeze-front development in areas where the flow is weakly onshore or parallel to the coast with land on the streamwise right. The secondary circulation induced by the frontogenetical process [see Bluestein (1985) for a review] and, in the case of the LBF1, condensational heating in cloud and precipitation bands that form aloft, likely intensifies the convergence and frontal collapse through a positive feedback loop, as suggested by numerical simulations (e.g., Ballentine 1982; Hjelmfelt and Braham 1983; Hjelmfelt 1990; Onton and Steenburgh 2001).

By 1800 UTC, daytime heating results in a reduced lake–air temperature contrast. This reduced contrast yields weaker diabatic heating by the boundary layer parameterization over Lake Ontario, including a weaker,
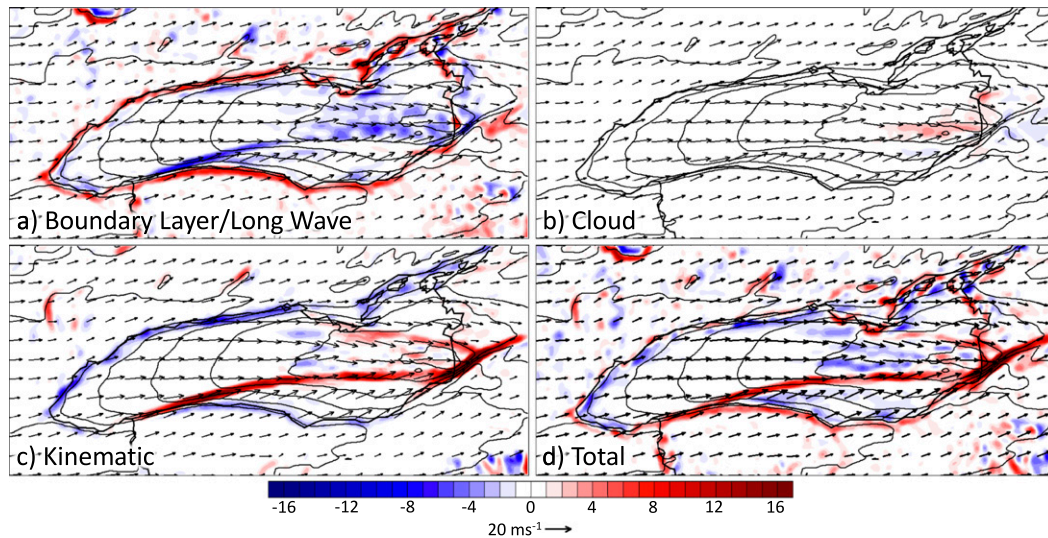
FIG. 9. WRF lowest-half-η-level potential temperature (contours every 1 K), wind (vectors following scale at bottom), and (a) diabatic frontogenesis produced by the boundary layer and longwave radiation parameterizations [K (10 km h)$^{-1}$ following scale at bottom], (b) diabatic frontogenesis produced by the cloud microphysics parameterization [as in (a)], (c) kinematic frontogenesis [as in (a)], and (d) total frontogenesis [as in (a)]. Potential temperature and frontogenesis smoothed with a seven-point cowbell spectral filter (Barnes et al. 1996) for clarity.

less organized, strip of high values near the shore (Fig. 10a). Longwave heating remains relatively unchanged (Fig. 10b), while the distribution of diabatic cooling produced by the cloud microphysics parameterization shifts slightly, but otherwise does not change significantly (Fig. 10c). The weaker diabatic heating maximum associated with the boundary layer parameterization results in weaker diabatic frontogenesis along the coast and frontolysis slightly offshore (Fig. 11a). Although the kinematic frontogenesis is also weaker (Fig. 11c), the total frontogenesis remains dominant along and downstream of the south shore bulge and southeast shore near Oswego.

7. Summary and conclusions

The above analysis illustrates how the large-scale flow, shoreline geometry of Lake Ontario, and differential surface heating and roughness influence the mesoscale forcing of lake-effect precipitation during OWLeS IOP2b. As summarized by Fig. 12, three major airmass boundaries developed in areas where the flow was onshore or parallel to the shore with land on the right. These areas include the south shore bulge between St. Catharines, Ontario, Canada, and Thirty Mile Point, New York; the southeast shore near Oswego, New York; and the north shore near Point Petre. Convergence and deformation in these shoreline regions reinforce the effects of differential diabatic heating, leading to frontogenesis and the development

of land-breeze fronts along the south shore bulge and southeast shore. Frontogenesis was also found in the convergence zone near and downstream of Point Petre, but was weaker and led to a less distinct baroclinic zone. Therefore, we classify this boundary as simply a convergence zone.

The land-breeze front and convergence zone along the south shore bulge (LBF1) separated from the shoreline near Thirty Mile Point, New York, extended downstream over eastern Lake Ontario, and served as the locus for development of the primary LLAP system. The land-breeze front along the southeast shore bulge (LBF2) extended downstream and obliquely across the LLAP system, influencing inland precipitation development over Tug Hill, as described in depth by Campbell and Steenburgh (2017). Convergence downstream of Point Petre produced an intermittent secondary lake-effect band to the north of the primary LLAP system.

Consistent with prior literature (e.g., Passarelli and Braham 1981; Schoenberger 1984; Hjelmfelt 1990; Grim et al. 2004), we have selected the term land-breeze front to describe the airmass boundaries that form along the south shore bulge and southeast shore, which feature strong horizontal potential temperature gradients. These two airmass boundaries, however, differ from classical land-breeze fronts in several ways. First, rather than being a component of the diurnal land/sea-breeze system that develops at night in response to radiational cooling over land, they form in response to differential
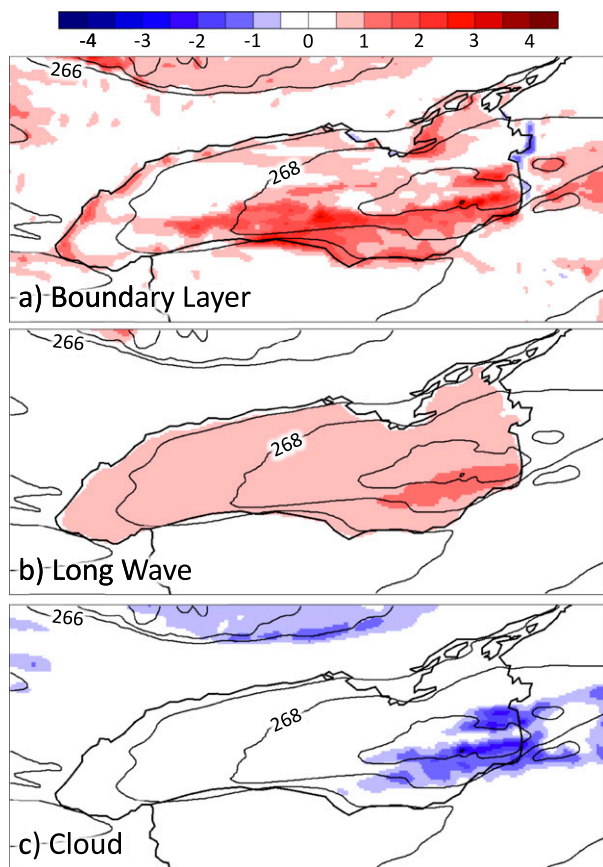
FIG. 10. As in Fig. 8, but at 1800 UTC 11 Dec.

it during the day (e.g., Fig. 6), however, during IOP2b, the coastal temperature gradient never reversed as one might expect during the day. Second, the large-scale flow was primarily alongshore, allowing convergence generated by differential roughness to serve as a contributor for land-breeze-front development. Indeed, the two land-breeze fronts share many characteristics with coastal fronts, which typically form in response to several effects related to orography, coastal geometry, land–sea heating contrasts, and differential roughness (e.g., Bosart et al. 1972; Bosart 1975). Finally, streamwise advection of the strong temperature gradients that developed in the two shoreline regions enables the land-breeze fronts to extend downstream and, in the case of the land-breeze front along the southeast shore, inland and across Tug Hill.

The structure and contributions of the airmass boundaries described above is more complex than that depicted by contemporary conceptual models of lake-effect systems produced by elongated lakes, which typically emphasize symmetrical land breezes that converge near the midlake axis [e.g., Lackmann (2011), his Fig. 9.19; Steenburgh (2014), his Fig. 5.5]. It is unclear, however, how broadly that the three-boundary structure of IOP2b applies to other LLAP system events over Lake Ontario or in other regions. It is likely that in other events over Lake Ontario there is sensitivity to the strength and direction of the large-scale flow, lake–land temperature contrast, and other factors, whereas the differing shoreline geometries of other bodies of water would also play a role. Nevertheless, we note that Holroyd (1971) distinguished between "friction induced" lake-effect bands that formed near the south shore bulge of Lake Ontario and

diabatic heating driven primarily by the movement of cold air over Lake Ontario. The diurnal heating and cooling cycle plays a secondary role by strengthening the lake–land temperature gradient at night and weakening
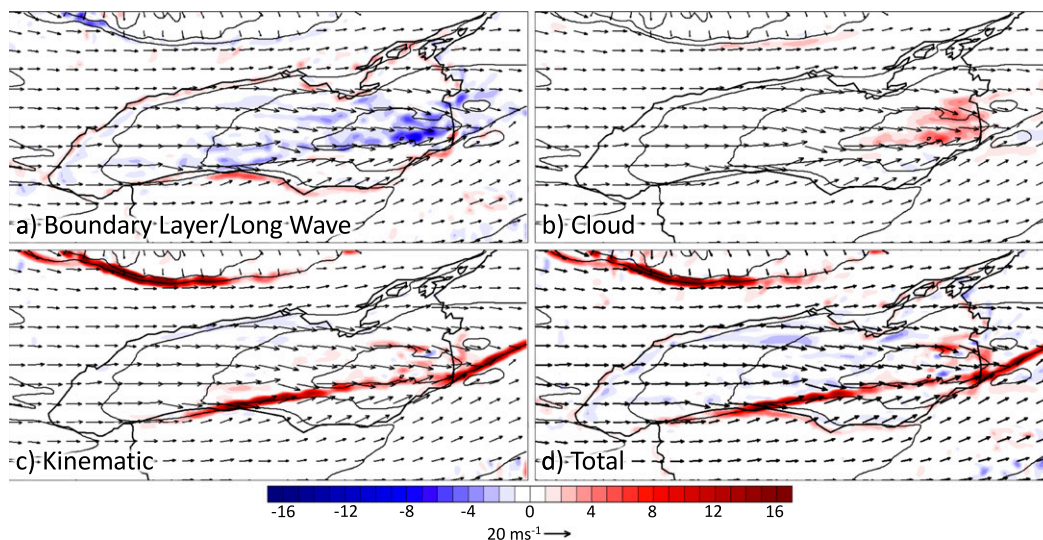
FIG. 11. As in Fig. 9, but at 1800 UTC 11 Dec.
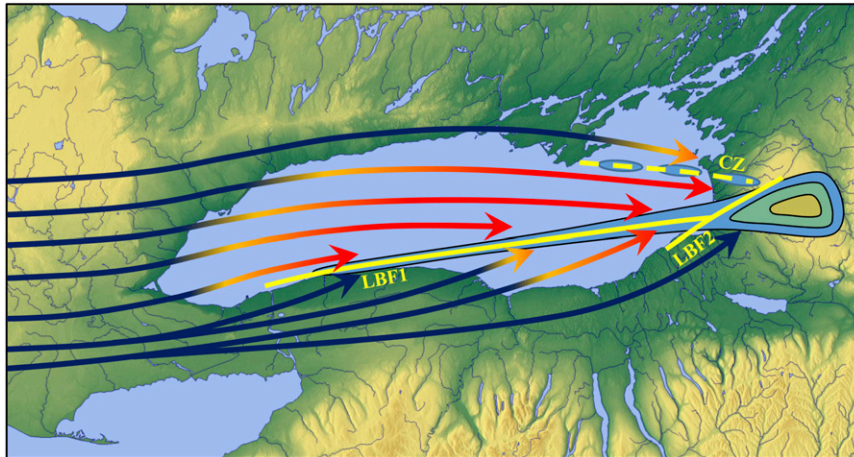
FIG. 12. Schematic summary of the mesoscale forcing of lake-effect precipitation during OWLeS IOP2b including 1) the land-breeze front (LBF1) generated along the south shore bulge, which plays a primary role in the LLAP system development; 2) the land-breeze front (LBF2) generated along the southeast shore, which cuts obliquely across the LLAP system and influences inland precipitation process; and 3) the convergence zone (CZ) downstream of Point Petre, which contributes to intermittent secondary LLAP system development. Color-filled arrows indicate major airstreams and lake modification of temperatures.

"thermally induced" bands that formed near the long-lake axis. We hypothesize that the structure of IOP2b likely represents a point in the continuum of LLAP systems that form over Lake Ontario. Improving the knowledge and simulation of the processes affecting the location and morphological characteristics (e.g., banded, nonbanded, double, or multiband) of LLAP system development is an important subject for future research as it is critical for predicting the location and intensity of lake-effect storms. Such work could employ quasi-idealized simulations with imposed wind conditions and lake geometries to further investigate the role of lake–land roughness contrasts and thermally forced circulations.

REFERENCES

Alcott, T. I., and W. J. Steenburgh, 2013: Orographic influences on a Great Salt Lake–effect snowstorm. *Mon. Wea. Rev.*, **141**, 2432–2450, doi:10.1175/MWR-D-12-00328.1.

Alestalo, M., and H. Savijärvi, 1985: Mesoscale circulations in a hydrostatic model: Coastal convergence and orographic lifting. *Tellus*, **37A**, 156–162, doi:10.1111/j.1600-0870.1985.tb00277.x.

Andersson, T., and N. Gustafsson, 1994: Coast of departure and coast of arrival: Two important concepts for the formation and structure of convective snowbands over seas and lakes. *Mon. Wea. Rev.*, **122**, 1036–1049, doi:10.1175/1520-0493(1994)122<1036:CODACO>2.0.CO;2.

Arritt, R. W., 1993: Effects of the large-scale flow on characteristic features of the sea breeze. *J. Appl. Meteor.*, **32**, 116–125, doi:10.1175/1520-0450(1993)032<0116:EOTLSF>2.0.CO;2.

Atlas, D., S.-H. Chou, and W. P. Byerly, 1983: The influence of coastal shape on winter mesoscale air–sea interaction. *Mon. Wea. Rev.*, **111**, 245–252, doi:10.1175/1520-0493(1983)111<0245:TIOCSO>2.0.CO;2.

Ballentine, R. J., 1982: Numerical simulation of land-breeze-induced snowbands along the western shore of Lake Michigan. *Mon. Wea. Rev.*, **110**, 1544–1553, doi:10.1175/1520-0493(1982)110<1544:NSOLBI>2.0.CO;2.

——, A. J. Stamm, E. E. Chermack, G. P. Byrd, and D. Schleede, 1998: Mesoscale model simulation of the 4–5 January 1995 lake-effect snowstorm. *Wea. Forecasting*, **13**, 893–920, doi:10.1175/1520-0434(1998)013<0893:MMSOTJ>2.0.CO;2.

Barnes, S. L., F. Caracena, and A. Marroquin, 1996: Extracting synoptic-scale diagnostic information from mesoscale models: The Eta model, gravity waves, and quasigeostrophic diagnostics. *Bull. Amer. Meteor. Soc.*, **77**, 519–528, doi:10.1175/1520-0477(1996)077<0519:ESSDIF>2.0.CO;2.

Benjamin, S. G., and Coauthors, 2016: A North American hourly assimilation and model forecast cycle: The Rapid Refresh. *Mon. Wea. Rev.*, **144**, 1669–1694, doi:10.1175/MWR-D-15-0242.1.

Bergmaier, P. T., B. Geerts, L. S. Campbell, and W. J. Steenburgh, 2017: The OWLeS IOP2b lake-effect snowstorm: Dynamics of the secondary circulation. *Mon. Wea. Rev.*, **145**, 2437–2459, doi:10.1175/MWR-D-16-0462.1.

Bluestein, H. B., 1985: Fronts and jet streaks: A theoretical perspective. *Mesoscale Meteorology and Forecasting*, P. S. Ray, Ed., Amer. Meteor. Soc., 173–215.

Bosart, L. F., 1975: New England coastal frontogenesis. *Quart. J. Roy. Meteor. Soc.*, **101**, 957–978, doi:10.1002/qj.49710143016.

——, C. J. Vaudo, and J. H. Helsdon Jr., 1972: Coastal frontogenesis. *J. Appl. Meteor.*, **11**, 1236–1258, doi:10.1175/1520-0450(1972)011<1236:CF>2.0.CO;2.

Brown, R. A., T. A. Niziol, N. R. Donaldson, P. I. Joe, and V. T. Wood, 2007: Improved detection using negative elevation angles for mountaintop WSR-88Ds. Part III: Simulations of shallow convective activity over and around Lake Ontario. *Wea. Forecasting*, **22**, 839–852, doi:10.1175/WAF1019.1.

Burt, C. A., 2007: *Extreme Weather*. 2nd ed. W. W. Norton and Company, 320 pp.

Campbell, L. S., and W. J. Steenburgh, 2017: The OWLeS IOP2b lake-effect snowstorm: Mechanisms contributing to the Tug Hill precipitation maximum. *Mon. Wea. Rev.*, **145**, 2461–2478, doi:10.1175/MWR-D-16-0461.1.

——, ——, P. G. Veals, T. W. Letcher, and J. R. Minder, 2016: Lake-effect mode and precipitation enhancement over the Tug Hill Plateau during OWLeS IOP2b. *Mon. Wea. Rev.*, **144**, 1729–1748, doi:10.1175/MWR-D-15-0412.1.

Case, J. L., M. M. Wheeler, J. Manobianco, J. W. Weems, and W. P. Roeder, 2005: A 7-yr climatological study of land breezes over the Florida Spaceport. *J. Appl. Meteor.*, **44**, 340–356, doi:10.1175/JAM-2202.1.

Chen, F., and J. Dudhia, 2001: Coupling an advanced land surface–hydrology model with the Penn State–NCAR MM5 modeling system. Part II: Preliminary model validation. *Mon. Wea. Rev.*, **129**, 587–604, doi:10.1175/1520-0493(2001)129<0587:CAALSH>2.0.CO;2.

Crosman, E. T., and J. D. Horel, 2010: Sea and lake breezes: A review of numerical studies. *Bound.-Layer Meteor.*, **137**, 1–29, doi:10.1007/s10546-010-9517-9.

Crum, T. D., R. L. Alberty, and D. W. Burgess, 1993: Recording, archiving, and using WSR-88D data. *Bull. Amer. Meteor. Soc.*, **74**, 645–653, doi:10.1175/1520-0477(1993)074<0645:RAAUWD>2.0.CO;2.

Davis, C. A., and W.-C. Lee, 2012: Mesoscale analysis of heavy rainfall episodes from SOWMEX/TIMREX. *J. Atmos. Sci.*, **69**, 521–537, doi:10.1175/JAS-D-11-0120.1.

Dudhia, J., 1989: Numerical study of convection observed during the Winter Monsoon Experiment using a mesoscale two-dimensional model. *J. Atmos. Sci.*, **46**, 3077–3107, doi:10.1175/1520-0469(1989)046<3077:NSOCOD>2.0.CO;2.

Grim, J. A., N. F. Laird, and D. A. R. Kristovich, 2004: Mesoscale vortices embedded within a lake-effect shoreline band. *Mon. Wea. Rev.*, **132**, 2269–2274, doi:10.1175/1520-0493(2004)132<2269:MVEWAL>2.0.CO;2.

Hjelmfelt, M. R., 1990: Numerical study of the influence of environmental conditions on lake-effect snowstorms over Lake Michigan. *Mon. Wea. Rev.*, **118**, 138–150, doi:10.1175/1520-0493(1990)118<0138:NSOTIO>2.0.CO;2.

——, and R. R. Braham, 1983: Numerical simulation of the airflow over Lake Michigan for a major lake-effect snow event. *Mon. Wea. Rev.*, **111**, 205–219, doi:10.1175/1520-0493(1983)111<0205:NSOTAO>2.0.CO;2.

Holroyd, E. W., 1971: Lake-effect cloud bands as seen from weather satellites. *J. Atmos. Sci.*, **28**, 1165–1170, doi:10.1175/1520-0469(1971)028<1165:LECBAS>2.0.CO;2.

Hong, S.-Y., Y. Noh, and J. Dudhia, 2006: A new vertical diffusion package with an explicit treatment of entrainment processes. *Mon. Wea. Rev.*, **134**, 2318–2341, doi:10.1175/MWR3199.1.

Iacono, M. J., J. S. Delamere, E. J. Mlawer, M. W. Shephard, S. A. Clough, and W. D. Collins, 2008: Radiative forcing by long-lived greenhouse gases: Calculations with the AER radiative transfer models. *J. Geophys. Res.*, **113**, D13103, doi:10.1029/2008JD009944.

Jiménez, P. A., J. Dudhia, J. F. González-Rouco, J. Navarro, J. P. Montávez, and E. García-Bustamante, 2012: A revised scheme for the WRF surface layer formulation. *Mon. Wea. Rev.*, **140**, 898–918, doi:10.1175/MWR-D-11-00056.1.

Kain, J. S., 2004: The Kain–Fritsch convective parameterization: An update. *J. Appl. Meteor.*, **43**, 170–181, doi:10.1175/1520-0450(2004)043<0170:TKCPAU>2.0.CO;2.

Kristovich, D. A. R., N. F. Laird, and M. R. Hjelmfelt, 2003: Convective evolution across Lake Michigan during a widespread lake-effect snow event. *Mon. Wea. Rev.*, **131**, 643–655, doi:10.1175/1520-0493(2003)131<0643:CEALMD>2.0.CO;2.

——, and Coauthors, 2017: The Ontario Winter Lake-Effect Systems field campaign: Scientific and educational adventures to further our knowledge and prediction of lake-effect storms. *Bull. Amer. Meteor. Soc.*, **98**, 315–332, doi:10.1175/BAMS-D-15-00034.1.

Kunkel, K. E., N. E. Westcott, and D. A. R. Kristovich, 2002: Effects of climate change on heavy lake-effect snowstorms near Lake Erie. *J. Great Lakes Res.*, **28**, 521–536, doi:10.1016/S0380-1330(02)70603-5.

Lackmann, G., 2011: *Midlatitude Synoptic Meteorology: Dynamics, Analysis, and Forecasting*. Amer. Meteor. Soc., 345 pp.

Laird, N. F., J. E. Walsh, and D. A. R. Kristovich, 2003a: Model simulations examining the relationship of lake-effect morphology to lake shape, wind direction, and wind speed. *Mon. Wea. Rev.*, **131**, 2102–2111, doi:10.1175/1520-0493(2003)131<2102:MSETRO>2.0.CO;2.

——, D. A. R. Kristovich, and J. E. Walsh, 2003b: Idealized model simulations examining the mesoscale structure of winter lake-effect circulations. *Mon. Wea. Rev.*, **131**, 206–221, doi:10.1175/1520-0493(2003)131<0206:IMSETM>2.0.CO;2.

Lavoie, R. L., 1972: A mesoscale numerical model of lake-effect storms. *J. Atmos. Sci.*, **29**, 1025–1040, doi:10.1175/1520-0469(1972)029<1025:AMNMOL>2.0.CO;2.

Lee, J.-G., and M. Xue, 2013: A study on a snowband associated with a coastal front and cold-air damming event of 3–4 February 1998 along the eastern coast of the Korean Peninsula. *Adv. Atmos. Sci.*, **30**, 263–279, doi:10.1007/s00376-012-2088-6.

Markowski, P., and Y. Richardson, 2010: *Mesoscale Meteorology in Midlatitudes*. Wiley-Blackwell, 407 pp.

Mazon, J., S. Niemelä, D. Pino, H. Savijärvi, and T. Vihma, 2015: Snow bands over the Gulf of Finland in wintertime. *Tellus*, **67A**, 25102, doi:10.3402/tellusa.v67.25102.

McMillen, J. D., and W. J. Steenburgh, 2015: Capabilities and limitations of convection-permitting WRF simulations of lake-effect systems over the Great Salt Lake. *Wea. Forecasting*, **30**, 1711–1731, doi:10.1175/WAF-D-15-0017.1.

Miller, J. E., 1948: On the concept of frontogenesis. *J. Meteor.*, **5**, 169–171, doi:10.1175/1520-0469(1948)005<0169:OTCOF>2.0.CO;2.

Miller, S. T. K., B. D. Keim, R. W. Talbot, and H. Mao, 2003: Sea breeze: Structure, forecasting, and impacts. *Rev. Geophys.*, **41**, 1011, doi:10.1029/2003RG000124.

Minder, J. R., T. W. Letcher, L. S. Campbell, P. G. Veals, and W. J. Steenburgh, 2015: The evolution of lake-effect convection during landfall and orographic uplift as observed by profiling radars. *Mon. Wea. Rev.*, **143**, 4422–4442, doi:10.1175/MWR-D-15-0117.1.

Norris, J., G. Vaughan, and D. M. Schultz, 2013: Snowbands over the English Channel and Irish Sea during cold-air outbreaks. *Quart. J. Roy. Meteor. Soc.*, **139**, 1747–1761, doi:10.1002/qj.2079.

Norton, D. C., and S. J. Bolsenga, 1993: Spatiotemporal trends in lake effect and continental snowfall in the Laurentian Great Lakes, 1951–1980. *J. Climate*, **6**, 1943–1956, doi:10.1175/1520-0442(1993)006<1943:STILEA>2.0.CO;2.

Onton, D. J., and W. J. Steenburgh, 2001: Diagnostic and sensitivity studies of the 7 December 1998 Great Salt Lake–effect snowstorm. *Mon. Wea. Rev.*, **129**, 1318–1338, doi:10.1175/1520-0493(2001)129<1318:DASSOT>2.0.CO;2.

Passarelli, R. E., and R. R. Braham, 1981: The role of the winter land breeze in the formation of Great Lake snow storms. *Bull. Amer. Meteor. Soc.*, **62**, 482–492, doi:10.1175/1520-0477(1981)062<0482:TROTWL>2.0.CO;2.

Peace, R. L., and R. B. Sykes, 1966: Mesoscale study of a lake effect snow storm. *Mon. Wea. Rev.*, **94**, 495–507, doi:10.1175/1520-0493(1966)094<0495:MSOALE>2.3.CO;2.

Petterssen, S., 1936: Contribution to the theory of frontogenesis. *Geofys. Publ.*, **11** (6), 1–27.

Reinking, R. F., and Coauthors, 1993: The Lake Ontario Winter Storms (LOWS) Project. *Bull. Amer. Meteor. Soc.*, **74**, 1828–1828, doi:10.1175/1520-0477-74-10-1828.

Savijärvi, H. I., 2012: Cold air outbreaks over high-latitude sea gulfs. *Tellus*, **64A**, 12244, doi:10.3402/tellusa.v64i0.12244.

——, 2015: Cold air outbreaks along a non-frozen sea channel: Effects of wind on snow bands. *Meteor. Atmos. Phys.*, **127**, 383–391, doi:10.1007/s00703-015-0370-8.

Schmidlin, T. W., 1993: Impacts of severe winter weather during December 1989 in the Lake Erie snowbelt. *J. Climate*, **6**, 759–767, doi:10.1175/1520-0442(1993)006<0759:IOSWWD>2.0.CO;2.

Schoenberger, L. M., 1984: Doppler radar observation of a land-breeze cold front. *Mon. Wea. Rev.*, **112**, 2455–2464, doi:10.1175/1520-0493(1984)112<2455:DROOAL>2.0.CO;2.

Schroeder, J. J., D. A. R. Kristovich, and M. R. Hjelmfelt, 2006: Boundary layer and microphysical influences of natural cloud seeding on a lake-effect snowstorm. *Mon. Wea. Rev.*, **134**, 1842–1858, doi:10.1175/MWR3151.1.

Smith, T. L., S. G. Benjamin, J. M. Brown, S. S. Weygandt, T. G. Smirnova, and B. E. Schwartz, 2008: Convection forecasts from the hourly updated, 3-km High Resolution Rapid Refresh (HRRR) model. *24th Conf. on Severe Local Storms*, Savannah, GA, Amer. Meteor. Soc., 11.11. [Available online at https://ams.confex.com/ams/24SLS/techprogram/paper_142055.htm.]

Steenburgh, J., 2014: *Secrets of the Greatest Snow on Earth.* Utah State University Press, 186 pp.

Steiger, S. M., and Coauthors, 2013: Circulations, bounded weak echo regions, and horizontal vortices observed within long-lake-axis-parallel–lake-effect storms by the Doppler on Wheels. *Mon. Wea. Rev.*, **141**, 2821–2840, doi:10.1175/MWR-D-12-00226.1.

Thompson, G., P. R. Field, R. M. Rasmussen, and W. D. Hall, 2008: Explicit forecasts of winter precipitation using an improved bulk microphysics scheme. Part II: Implementation of a new snow parameterization. *Mon. Wea. Rev.*, **136**, 5095–5115, doi:10.1175/2008MWR2387.1.

Veals, P. G., and W. J. Steenburgh, 2015: Climatological characteristics and orographic enhancement of lake-effect precipitation east of Lake Ontario and over the Tug Hill Plateau. *Mon. Wea. Rev.*, **143**, 3591–3609, doi:10.1175/MWR-D-15-0009.1.

Welsh, D., B. Geerts, X. Jing, P. T. Bergmaier, J. R. Minder, W. J. Steenburgh, and L. S. Campbell, 2016: Understanding heavy lake-effect snowfall: The vertical structure of radar reflectivity in a deep snowband over and downwind of Lake Ontario. *Mon. Wea. Rev.*, **144**, 4221–4244, doi:10.1175/MWR-D-16-0057.1.